Large-Scale Inverse Ku-Band Backscatter Modeling of Sea Ice

Quinn P. Remund, *Member, IEEE*, and David G. Long, *Senior Member, IEEE*

***Abstract*—Polar sea ice characteristics provide important inputs to models of several geophysical processes. Microwave scatterometers are ideal for monitoring these regions due to their sensitivity to ice properties and insensitivity to atmospheric distortions. Many forward electromagnetic scattering models have been proposed to predict the normalized radar cross section (σ°) from sea ice characteristics. These models are based on very small scale ice features and generally assume that the region of interest is spatially homogeneous. Unfortunately, spaceborne scatterometer footprints are very large (5–50 km) and usually contain very heterogeneous mixtures of sea ice surface parameters. In this paper, we use scatterometer data in a large-scale inverse modeling experiment. Given the limited data resolution, we adopt a simple geometric optics forward-scattering model to analyze surface and volume scattering contributions to observed Ku-band signatures. A model inversion technique based on recursive optimization of an objective function is developed. The result is a least squares estimate of three surface parameters: the power reflection coefficient at nadir, the rms surface slope, and the volume scattering albedo. Simulations demonstrate the performance of the method in the presence of noise. The inverse model is implemented using Ku-band image reconstructed data collected by the National Aeronautics and Space Administration scatterometer. The results are used to analyze and interpret σ° phenomena occurring in the Antarctic and the Arctic.**

***Index Terms*—Inverse modeling, National Aeronautics and Space Administration (NASA) Scatterometer (NSCAT), scattering models, sea ice, Special Sensor Microwave/Imager (SSM/I).**

I. Introduction

THE CRYOSPHERE regions of the earth play a critical role in many global geophysical processes. In particular, polar sea ice packs are important in understanding weather patterns and climate trends. Sea ice influences heat exchange, fresh water exchange, and the absorption of solar radiation and is believed to be a sensitive indicator of long-term climate trends [1], [2]. Consequently, the remote sensing community has great interest in monitoring these important regions. The primary goal of cryosphere remote sensing is the extraction of key sea ice surface characteristics from the observed signatures.

A wide array of spaceborne instruments has been employed in past and current efforts to study and monitor the cryosphere. The various instruments cover a broad spectrum of frequencies, polarizations, spatial resolutions, and measurement collection schemes. Microwave remote sensing instruments have proven extremely valuable in observing the polar regions. Active microwave instruments exhibit low sensitivity to cloud cover, precipitation, and other forms of atmospheric distortion in the polar regions, but significant sensitivity to sea ice characteristics. Because active weather patterns in the polar regions often result in heavy cloud cover during a significant portion of the annual weather cycle, and polar winters are characterized by long seasons of continuous darkness, optical sensors can be difficult to apply. Unlike optical instruments, microwave sensors do not depend upon solar illumination to collect measurements.

Several satellite instruments have proven the utility of scatterometers in monitoring the Arctic and Antarctic regions. The first was the Seasat-A Scatterometer (SASS). Though the SASS mission was short, SASS data illustrated that Ku-band measurements are sensitive to the presence of sea ice and show valuable variations within the ice pack that relate to surface features [3]–[6]. Later, the Active Microwave Instrumentation (AMI) scatterometers aboard the European Remote Sensing 1 and 2 (ERS-1 and ERS-2) satellites demonstrated the value of C-band active scatterometer data in monitoring sea and glacial ice regions [4], [7], [8]. The National Aeronautics and Space Administration (NASA) Scatterometer (NSCAT) flew aboard the Advanced Earth Observation Satellite (ADEOS) platform from approximately August 1996 through June 1997. Ku-band NSCAT data have been used in a number of cryosphere studies [4], [9]–[11]. When the NSCAT mission was prematurely terminated due to a solar panel failure, the NASA-built SeaWinds instrument aboard QuikSCAT filled the gap of active Ku-band data in mid-1999. SeaWinds data is used to monitor sea ice extent [12].

II. NSCAT Instrument and Image Reconstruction

Microwave σ° signatures of sea ice contain important information about surface characteristics [13]. The goal of inverse modeling is to extract or estimate those parameters from σ° measurements. The observed signatures are also a function of instrument design and measurement collection specifications such as frequency, polarization, and incidence angle [14]–[18]. This section describes the instrument used in this paper for measurement collection and the image reconstruction algorithms that produce enhanced resolution imagery. These images function as inputs to the inverse model of Section IV.

NSCAT has a number of characteristics that make it useful in monitoring sea ice [10]. It is a dual-polarization Ku-band scatterometer operating at approximately 14 GHz. NSCAT employs six v-pol and two h-pol fan beams that measure the normalized radar cross section (σ°) at various azimuth angles [19]. The beams are further resolved through Doppler filtering, resulting

Manuscript received January 21, 2001; revised March 6, 2003.

Q. P. Redmund is with Ball Aerospace and Technologies Corporation, Boulder, CO 80301 USA.

D. G. Long is with the Department of Electrical and Computer Engineering, Brigham Young University, Provo, UT 84602 USA.

Digital Object Identifier 10.1109/TGRS.2003.813495

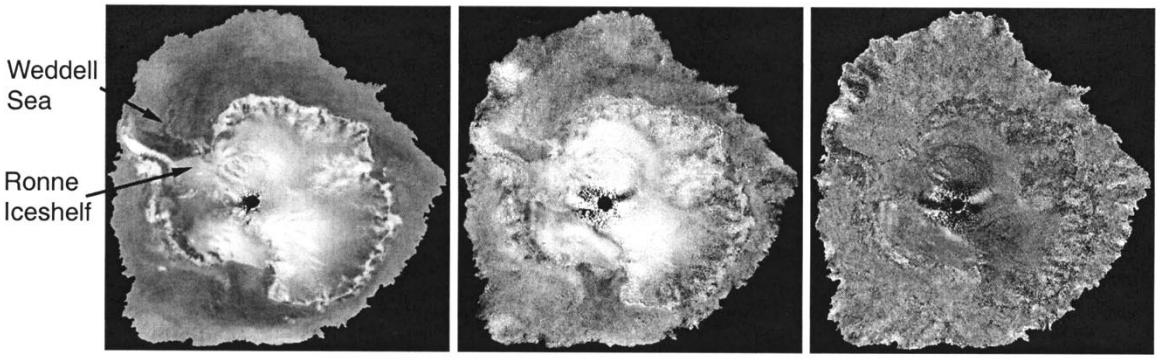

Fig. 1. Sample ice-masked NSCAT AVE v-pol imagery for 1996 days 270–275. The images are, from Sleft to right, A_v, B_v, and C_v, respectively. The original images contain 1940 $\times$ 1940 pixels with a nominal pixel spacing of 4.45 km.

in a number of measurement cells within each fan beam footprint. The cells have various incidence angles with a nominal spatial resolution of about 25 km. Observations at multiple incidence angles allow for the estimation of incidence angle dependence—an important factor in determining surface characteristics. Furthermore, dual-polarization measurements allow for the determination of the polarization response of sea ice.

Multiple NSCAT passes over the polar regions are used to reconstruct σ° imagery. To improve the nominal resolution of NSCAT measurements, resolution enhancement algorithms can be applied to generate images. These methods rely upon a parameterization of the dependence of σ° on incidence angles. Various-order models can be used with increasing sensitivity to noise as order is increased. In general, σ° (in decibels) can be modeled by

$$\sigma^\circ \text{ (dB)} = A + B(\theta - 40^\circ) + C(\theta - 40^\circ)^2 + D(\theta - 40^\circ)^3 + \cdots \quad (1)$$

where θ is the incidence angle; A is σ° normalized to 40°; B is the linear incidence angle dependence of σ°; C is the quadratic incidence angle dependence of σ°, and so forth. For a limited range of incidence angles of 20° and 60°, NSCAT σ° is found to have a nearly linear dependence on θ. Higher order models can be used to more accurately represent the dependence though the higher coefficients become increasingly sensitive to noise.

Several reconstruction methods exist for the generation of scatterometer imagery. For this study, a polar stereographic projection was used in all image products. The first reconstruction method consists of binning σ° measurements into 22.25 $\times$ 22.25-km grid cells. For each cell, a polynomial fit of a chosen order is applied to model the θ dependence of σ°. Hence, $N+1$ binned images are produced where N is the polynomial order. Since the nominal NSCAT resolution is 25 km, this technique does not improve measurement resolution but is less prone to reconstruction artifacts and noise.

The AVE algorithm is another reconstruction technique for scatterometer image production [20]. Like the binning method, a polynomial fit is used for each pixel to estimate the pertinent coefficients. However, the AVE method uses a higher resolution 4.45 $\times$ 4.45-km grid and produces images with an effective resolution of 12–15 km. For a particular pixel, the polynomial fit measurement set consists of all the measurements whose spatial footprint response include that pixel. AVE images are produced for each polynomial coefficient. Sample ice-masked AVE images of the Antarctic during 1996, days 270–275 are shown in Fig. 1 in which a second-order model was employed. The images are ice masked using an NSCAT-derived method described in [9]. Significant detail relating to surface parameters is evident in varying A, B, and C pixel values. The images also demonstrate that higher order terms are increasingly sensitive to measurement and reconstruction noise.

The final image reconstruction method is the scatterometer image reconstruction (SIR) algorithm [20]. SIR is a modified multivariate multiplicative algebraic reconstruction technique that uses multiple passes of a satellite instrument to increase spatial resolution [21]. Like the AVE algorithm, a 4.45-km nominal pixel spacing is used. SIR reconstructed images produce an effective resolution of approximately 10 km instead of the nominal 25–50-km resolution of the instrument [22]. SIR results in increased reconstruction artifacts as well as increased resolution. For this reason, only the first-order σ° versus θ model is used for SIR imagery.

Each of the described reconstruction algorithms have inherent strengths and weaknesses. The binning images have the lowest resolution, but less noise in higher order coefficients. The AVE images have medium resolution with somewhat higher noise levels. The SIR reconstructed images have the highest resolution but are more sensitive to noise in the high-order coefficients. For the Antarctic and Arctic regions, all of these methods require six days included in the image generation to achieve full v- and h-pol coverage with a range of incidence angles in each pixel. Ice motion during the imaging interval can cause blurring in the final image products particularly in the AVE and SIR images.

III. Large-Scale Forward Modeling of Sea Ice Backscatter

Forward models of sea ice backscatter have been developed that predict σ° as a function of incidence angle and important surface parameters. Various sea ice characteristics affect observed signatures. For example, surface roughness reduces specular reflections and increases backscatter. Geophysically, this parameter is important in modulating wind shearing forces on the ice pack and can be an indicator of internal stresses.

Liquid water content also influences backscatter signatures. Increased water content results in less penetration by incident microwave pulses. Hence, the backscatter is dominated by the surface scattering response. Snow cover adds another layer to the multilayer structure. Very dry snow appears electrically transparent at many microwave frequencies. However, as snow liquid water content increases, the sea ice signature is increasingly masked. In addition, sea ice salinity plays a role in determining backscatter responses. Brine pockets increase the effective permittivity and provide volume scattering elements. Since brine pockets are commonly ellipsoidal in shape, the orientation of these inclusions influences the σ° polarization response. Both snow cover and brine pocket distribution are closely related to sea ice age. Older ice forms typically have greater accumulated snow cover. Also, sea ice aging results in increased brine drainage. Volume scattering air bubbles often remain in the place of old brine inclusions.

A better understanding of scattering from sea ice enhances the ability to estimate geophysical parameters through inverse modeling. Current research in the field has focused on mathematically modeling the complex process of scattering from sea ice on small scales as a function of the previously described parameters. The complexity is due in part to the anisotropic nature sea ice permittivities. A particular source of anisotropy is the vertically oriented brine pockets caught within the ice crystal lattice. In addition, sea ice is a multilayer medium with rough surface and volume scattering contributions to the backscatter signature. Multilayer anisotropic scattering models have been proposed using a dyadic Green's function as well as the first-order Born approximation to predict backscatter coefficients [23]. Tjuatja *et al.* developed a scattering model for snow-covered sea ice using radiative transfer theory [24]. While several radiative transfer techniques have been proposed in the past, Tjuatja's model is considerably more robust by accounting for non-Rayleigh particle sizes and close spacing between scatterers. An example of sea ice forward-scatter modeling is the work of Nghiem *et al.* [25] in which a polarimetric backscattering model is derived. Nghiem relates ice, brine, air, and salinity properties to backscatter signatures.

Several factors limit the use of such models in large-scale inversion studies. First, the wide seasonal and spatial variability in the dielectric and large-scale surface roughness properties of the ice hamper the interpretation of the backscatter maps. Second, the detailed ice scattering models models assume the region of interest has relatively homogeneous scattering properties. Some randomness is allowed in the form of random surface height or other parameters with specified variances but, in general, the region is considered to be spatially homogeneous. This may be appropriate for SAR imagery where the resolution is a few tens of meters, but scatterometer footprints have 5–50-km resolution and thus can often cover very heterogeneous regions. Also, the detailed models are very computationally complex. Inversion of the models on large fields of measurements is not computationally feasible. Consequently, a model for use at the lower resolution found in scatterometer imagery must be based on more general, average, large-scale parameters. Computational complexity of the forward model must be simple enough to allow for inversions of large data sets in relatively short time frames. One such simple model assumes that sea ice scattering consists of incoherently summed surface and volume scattering responses [26]–[28]

$$\sigma_m^\circ = \sigma_s^\circ + \sigma_v^\circ$$
$$\sigma_m^\circ = \sigma_s^\circ + t^2\left(\frac{n\sigma_b}{2\alpha}\right)\cos\theta_i \tag{2}$$

where

- σ_m° measured σ°;
- σ_s° surface scattering σ°;
- σ_v° volume scattering σ°,
- θ_i measurement incidence angle;
- t plane wave power transmission coefficient at $\theta = \theta_i$;
- n number density of subsurface scattering elements;
- σ_b σ° per particle;
- α volume attenuation coefficient.

This bulk model does not require a detailed description of the ice medium. Instead, several large-scale parameters are used to represent the mean response in the region of interest. Following Swift [27] three primary volume scattering parameters are combined into one variable, the volume scatter albedo given by

$$\eta = \frac{n\sigma_b}{\alpha}. \tag{3}$$

Though it is a general parameter, η is related to sea ice features such as the number of volume scattering brine pockets and air bubbles. It is also sensitive to the effective permittivity of the sea ice layers below the surface. Highly saline brine pockets have higher σ_b than air bubbles resulting in greater η values for the same number density, n.

This simple volume scattering model assumes only single scattering. While multiple scattering certainly occurs in a sea ice medium, the model assumes these are negligible compared to the direct backscatter response. Fig. 2 shows v-pol volume backscatter as a function of incidence angle for various η values. The signatures exhibit low dependence on incidence angle. As η increases, the level of σ° also rises. Volume scattering occurs primarily in ice types containing numerous inhomogeneities and low loss such as multiyear ice. Snow layers containing crystallized structures can also result in strong volume scattering contributions. Hence, in the model inversion, we expect multiyear ice forms to have relatively high η when compared with younger ice types such as first-year ice.

Surface scattering is also an integral component of the backscatter model. Assuming that the surface can be modeled as an ensemble of reflective facets with Gaussian slope distributions, a geometric optics solution can be used [27], [29] so that

$$\sigma_s^\circ = \frac{r(0)e^{-\tan^2\theta_i/2S^2}}{2S^2\cos^4\theta_i} \tag{4}$$

where $r(0) = 1 - t(0)$ is the surface power reflection coefficient at nadir and S is the rms surface slope.The geometric optics solution is derived under the assumption that the wavelength is significantly smaller than the typical roughness dimensions. At 14 GHz, the corresponding wavelength is approximately 2.1 cm. Hence, the model accounts for roughness features that are much larger than this, while smaller roughnesses may not be fully accounted for in the model. We expect that large surface roughness

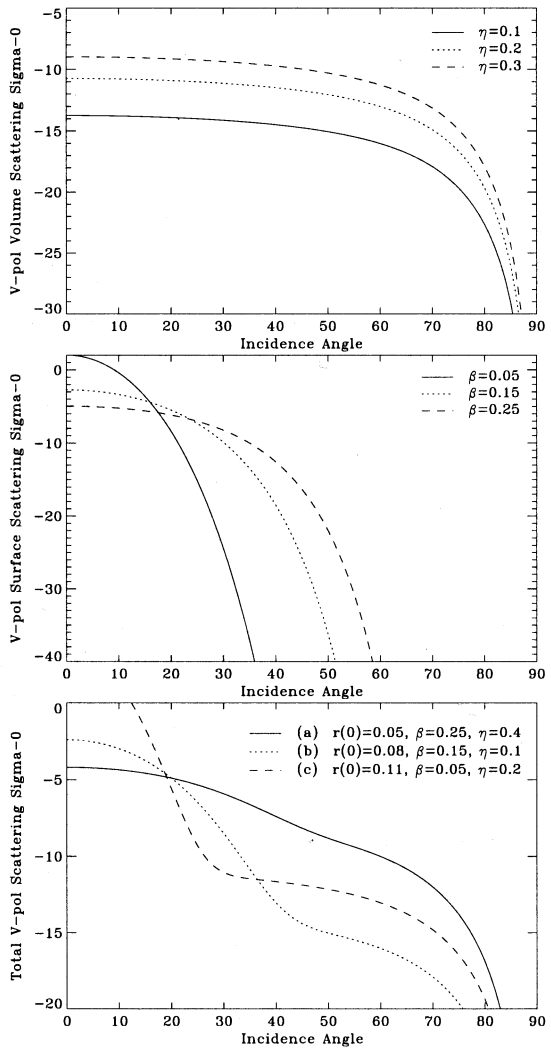

Fig. 2. Model-generated volume scattering v-pol σ° responses versus incidence angle. Volume scattering responses as a function of η are shown in the top frame. Surface scattering as a function of $\beta = 2S^2$ is shown in the middle assuming $r(0) = 0.08$ corresponding to a dielectric constant of 3.2. The bottom frame illustrates three total scattering examples.

due to wave action, ice pack shearing forces, and ridges are well within the bounds of this assumption. However, very small-scale roughness due to such phenomena as wind roughening of open water and melt ponds and very small surface inhomogeneities are not accounted for in the model.

For the purposes of this paper, we define $\beta = 2S^2$ to simplify the model inversion. Fig. 2 illustrates the theoretical v-pol scattering responses for various values of β. The plots show that as surface slope increases, the σ° response broadens in incidence angle. For very smooth surfaces, a significant portion of the response occurs below 20° incidence. Since 20° is used as the lower cutoff for the NSCAT measurements used in the image reconstructions, we expect that the inversion will have limited capability in accurately identifying very low β.

At Ku-band, surface scattering dominates young and first-year ice responses that have relatively high water and brine content. These types have significant conductivity and, hence, high loss. Surface melting masks lower level volume scattering and creates greater relative dependence on surface scattering contributions. Inverse modeling of σ° images should result in relatively high β in regions of significant surface deformation and low values over smoother ice forms.

The two fundamental parameters in the surface scatter model, $r(0)$ and β, are both related to important surface features. The Fresnel reflectivity coefficient, $r(0)$, is directly related to the effective permittivity of sea ice. It has been shown that lossless sea ice permittivities are roughly between 3.0 and 4.5 [26], [30] in the Ku-band portion of the spectrum resulting in $r(0)$ values within the range of 0.072–0.13. However, the forward model assumes that the sea ice is lossless. While this applies reasonably well for older ice forms such as ice bergs and multiyear ice in winter, internal water content or surface melt introduces conductivity and loss to the medium. Hence, dielectric constants should not be directly computed from estimates of $r(0)$ derived from the inverse model described in the following section. Nevertheless, $r(0)$ can be used to obtain a general idea of effective relative permittivities throughout the ice pack.

Fig. 2 shows the total scattering v-pol responses for sample $r(0)$, β, and η values. The plots illustrate that the theoretical σ° versus θ signatures can not always be fit with a linear approximation between 20° and 60°. A linear model is appropriate for plot a), but b) and c) clearly require higher order terms to accurately represent the incidence angle dependence. In general, the linear dependence assumption does not fit well in scenarios with relatively low β values. Swift was able to fit such plots to SASS σ° observations of multiyear ice in the Arctic [27], demonstrating the ability to invert the model and estimate the three fundamental parameters.

The three forward model parameters ($r(0)$, β, η) can be used as proxy values in the interpretation of polar imagery. We expect a close relationship to exist between these values and sea ice type. Consequently, the parameter estimates can be used in ice classification efforts.

IV. Model Inversion Methodology

The theoretical scattering model parameters, $r(0)$, β, and η can be estimated from observed NSCAT σ° signatures given sufficient incidence angle sampling. In this section, an automated inversion technique is presented for determining the three parameters from NSCAT reconstructed imagery.

The inversion approach consists of the automated steepest descent optimization of an objective function. The objective function provides a measure of the error between observed signatures and estimated model parameters

$$J\left(\sigma^\circ,\, r(0),\, \beta,\, \eta\right) = \sum_{\theta_i=20}^{60} \left[\sigma^\circ(\theta_i) - (\theta_i)\right]^2$$

$$J\left(\sigma^\circ,\, \vec{h}\right) = \sum_{\theta_i=20}^{60} \left[\sigma^\circ(\theta_i) - 10\log_{10} \cdot\left(\frac{r(0)e^{-\tan^2\theta_i/2S^2}}{2S^2\cos^4\theta_i} + t^2\left(\frac{\eta}{2}\right)\cos\theta_i\right)\right]^2 \quad (5)$$

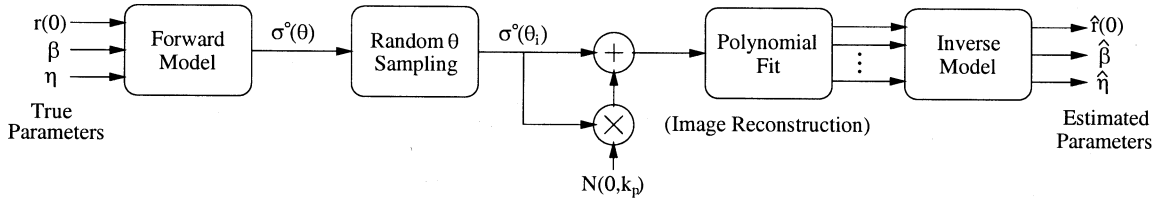

Fig. 3. Flowchart illustrating the inverse model simulation process.

where

J total squared modeling error;
$\sigma^\circ(\theta_i)$ observed backscatter cross section at θ_i;
$\sigma^\circ_m(\theta_i)$ modeled backscatter cross section at θ_i;
$\vec{h}$ vector of model parameters $[r(0), \beta, \eta]^T$.

Hence, $J(\sigma^\circ, \vec{h})$ is a measure of the accuracy of the model parameters in predicting the observed signature. The $\sigma^\circ(\theta_i)$ response is computed given the σ° versus θ variable-order polynomial fit coefficients for a particular pixel in the reconstructed imagery. Since total squared error is a sufficient statistic for mean squared error, the inversion method is a minimum mean squared error technique. Simulated three-dimensional objective functions (given an observed σ° signature) indicate that the function has a well defined minimum within the range of expected $r(0)$, β, and η. Hence, the optimal parameters are found at the $\vec{h}$ yielding minimum $J(\sigma^\circ, \vec{h})$.

One method of automated optimization of an objective function is the steepest descent approach. Steepest descent locates the minimum of a function in an iterative fashion through the estimation of the local slope. The slope is obtained from the partial derivatives of the objective function

$$G(\sigma^\circ, \vec{h}) = \left[-\frac{\partial}{\partial r(0)} J(\sigma^\circ, \vec{h}), -\frac{\partial}{\partial \beta} J(\sigma^\circ, \vec{h}), -\frac{\partial}{\partial \eta} J(\sigma^\circ, \vec{h})\right]^T \quad (6)$$

where $G(\sigma^\circ, \vec{h})$ is the direction vector. The partial derivatives in (6) are analytical functions of $\sigma^\circ(\theta)$, $r(0)$, β, and η given any location in the objective function. Consequently, $G(\sigma^\circ, \vec{h})$ can be computed for any location vector $\vec{h}$ and points in the direction of steepest descent.

A recursive algorithm for computing the model parameters, and thus searching for the minimum of $J(\sigma^\circ, \vec{h})$ is given by

$$\vec{h}(m+1) = \vec{h}(m) + \Delta(m) \odot G(m), \qquad m = 0, 1, 2, \ldots \quad (7)$$

where

Δ vector of step sizes for each model parameter;
$\odot$ Schur element by element vector product operator.

The step size Δ can be chosen in a number of ways. Steepest descent algorithms often use step sizes that are a function of the objective function. Hence, smaller steps are taken closer to the minimum. For this study, a fixed step size is used

$$\Delta = [0.001, \quad 0.002, \quad 0.002]^T \quad (8)$$

yielding model parameter estimate resolutions of 0.001, 0.002, and 0.002 for $r(0)$, β, and η, respectively.

The algorithm is initialized with arbitrary $\vec{h}(0)$. Simulations indicate that the minimum is found as long as $\vec{h}(0)$ is in the range of possible sea ice parameter values. For a given image set of polynomial fit coefficients, the algorithm is run for each pixel. The resulting products are images of $r(0)$, β, and η used in determining the spatial distribution of important surface parameters.

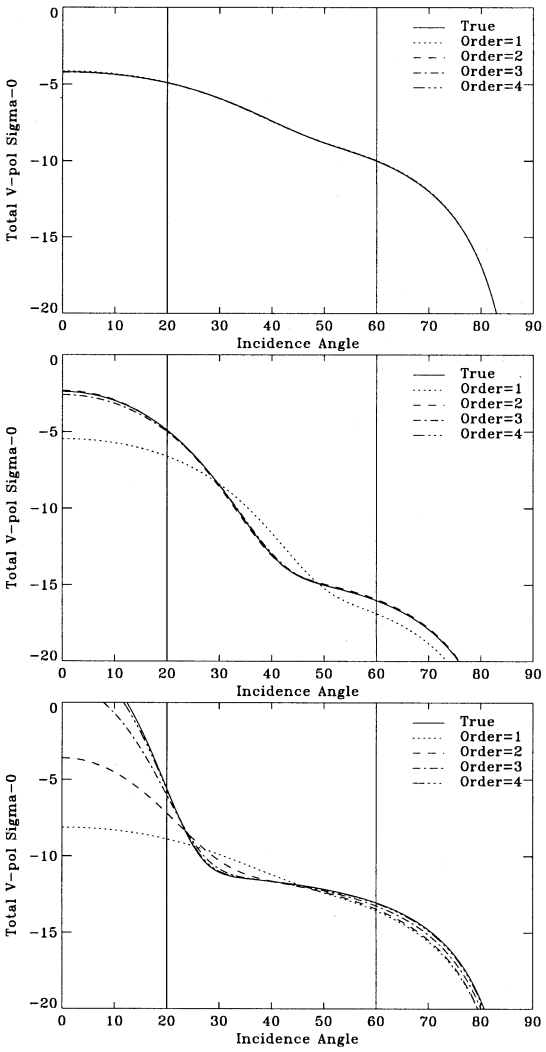

Fig. 4. Comparison of inverse model-derived responses at various orders with the true response from the three total scattering cases in Fig. 2. Case (a) (top), case (b) (middle), case (c) (bottom).

The algorithm has various strengths that make it useful in model inversion. First, the proposed algorithm is fully automated. Many previous inverse modeling studies focusing on fitting observed and forward modeled signatures have relied on user interaction to manually perturb the model parameters until a satisfactory match is obtained. The technique presented in this

TABLE I
INVERSE MODEL SIMULATION EXAMPLES IN THE ABSENCE OF NOISE AND WITH INCIDENCE ANGLE SAMPLING AT EACH DEGREE IN THE RANGE $\theta \in [20^\circ, 60^\circ]$

	Case (a)			Case (b)			Case (c)		
	r(0)	β	η	r(0)	β	η	r(0)	β	η
True	0.05	0.25	0.4	0.08	0.15	0.1	0.11	0.05	0.2
Order=1	0.049	0.242	0.404	0.06	0.242	0.082	0.015	0.222	0.178
Order=2	0.049	0.246	0.402	0.079	0.146	0.102	0.033	0.094	0.182
Order=3	0.05	0.252	0.4	0.078	0.154	0.1	0.073	0.06	0.19
Order=4	0.05	0.25	0.4	0.08	0.15	0.1	0.101	0.052	0.198

paper requires no user interaction and quickly estimates model parameters given an observed σ° versus θ response. This facilitates the production of model parameter image sequences from scatterometer imagery. In addition, if the σ° incidence angle dependence model is sufficient (of high enough order) the algorithm finds the best parameters in the minimum mean squared error sense.

The estimated parameters provide, in effect, the mean responses over the pixel region. These are useful on acroscopic level when viewing entire sea ice packs. We note that the products of the inversion technique have limited utility on very small scales. Because the model is based on a specific forward model, the quality of the resulting parameter estimates are directly related to the quality of the original forward model. We expect some error since the forward model does not account for such things as complex sea ice permittivities and small-scale roughness features.

V. INVERSE MODEL SIMULATIONS

To evaluate the capability of the inversion technique, simulations are designed and implemented. The simulation methodology is outlined in Fig. 3. First, the "ground truth" model parameters $r(0)$, β, and η are run through the forward model to produce a σ° versus θ response. This signature is then sampled in incidence angle between 20° and 60° to simulate scatterometer measurement collection. At this point, Monte Carlo scatterometer noise is added to each measurement using the noise model

$$\sigma_n^\circ(\theta_i) = \sigma^\circ(\theta_i)\,(1 + N(0,\, k_p)) \tag{9}$$

where

- $\sigma_n^\circ(\theta_i)$ noise-added σ° at incidence angle θ_i;
- $\sigma^\circ(\theta_i)$ original noiseless σ°;
- $N(0,\, k_p)$ normally distributed random variable with standard deviation k_p.

The noise-corrupted measurements are used to obtain polynomial fit coefficients. Variable degree polynomials are used to determine the effect of model order on the inversion. The coefficients are then input to the inverse model resulting in surface parameter estimates. Error analysis is performed with the original parameter values and the inverse model results.

For the purposes of illustration, we consider model inversion using the total scattering cases in Fig. 2. The inverse model is first evaluated in the absence of noise with ideal incidence angle sampling consisting of samples at each degree from 20° to 60°. For each case, the simulation is implemented using polynomial

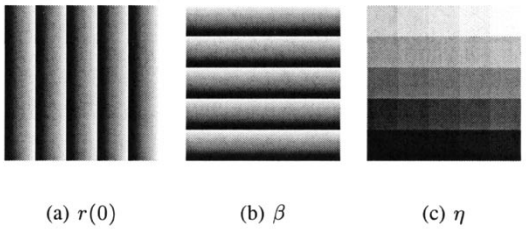

Fig. 5. "Truth" parameter images, $r(0)$, β, and η, used in the model simulations.

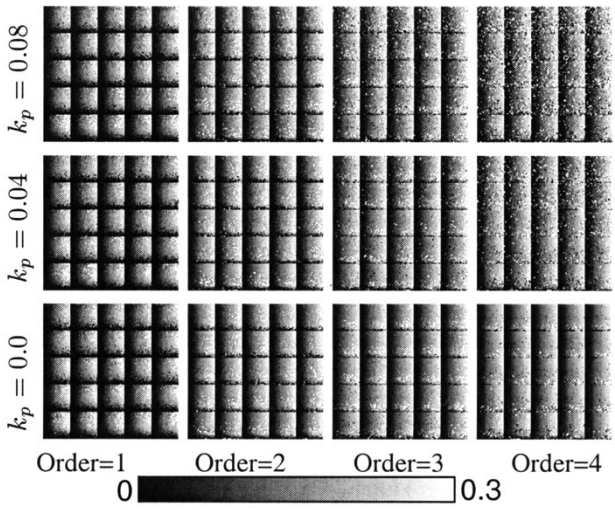

Fig. 6. Inverse model $r(0)$ parameter estimates at various σ° versus θ model orders and noise levels.

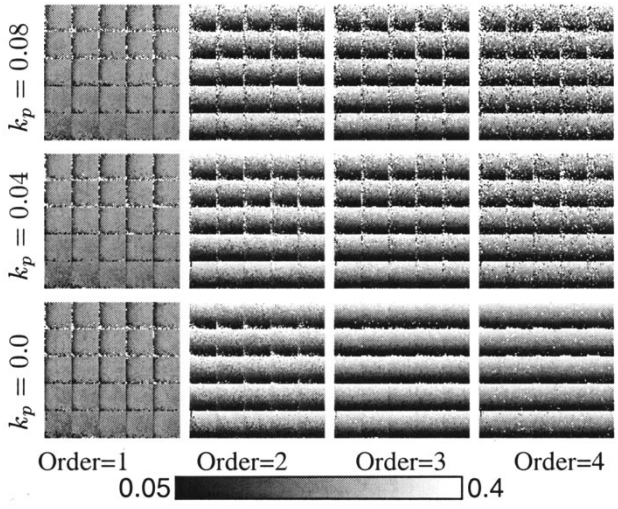

Fig. 7. Inverse model β parameter estimates at various σ° versus θ model orders and noise levels.

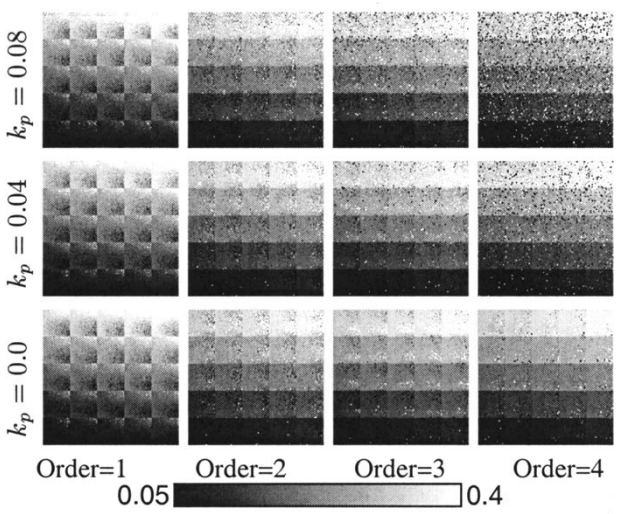

Fig. 8. Inverse model η parameter estimates at various σ° versus θ model orders and noise levels.

fit orders from one to four to illustrate the algorithm's performance. The first case to be inverted is example a) from Fig. 2. Table I contains the resulting estimates for all three parameters using different reconstruction model orders. These values demonstrate that virtually all polynomial orders provide good estimates of the true values. Since the response is close to linear in the 20° to 60° range that the inverse model considers, even the first-order model performs reasonably well. Fig. 4 shows a comparison of the true σ° signature with the estimated signatures at each of the considered orders. The vertical lines at 20° and 60° incidence angle bound the range over which the signature matching is performed. The plots are virtually indistinguishable demonstrating the proper performance of the algorithm.

The case (b) inversion illustrates the inverse model's performance with nonlinearities in the true σ° versus θ signature. In Table I it is evident that the first-order model performed poorly. The β estimate is particularly erroneous. However, at order two and above, the estimates are close to the actual values. Fig. 4 offers a graphical interpretation of the inversion case. The plots clearly show the poor performance of the first-order model values.

The true response in case (c) exhibits extreme nonlinearities. While we do not expect such a case to be common, it is included to show the inverse model's performance in extreme circumstances. For this scenario, third or fourth-order model coefficients are required as inputs to the inverse model to provide reasonable estimates of the surface parameters. Fig. 4 illuminates the situation further. These plots show the difficulty encountered by first and second-order inputs in matching the true signature. The sharp "elbow" in the response can only be accounted for by third– or fourth-order polynomial fits. A greater range of incidence angles included in the model would conceivably yield better estimates at all orders. Unfortunately, scatterometers like NSCAT do not collect measurements over such a broad range of viewing angles.

These three simulations demonstrate that the inverse model performs properly in the absence of noise given sufficient incidence angle sampling and satisfactory polynomial fit coefficient

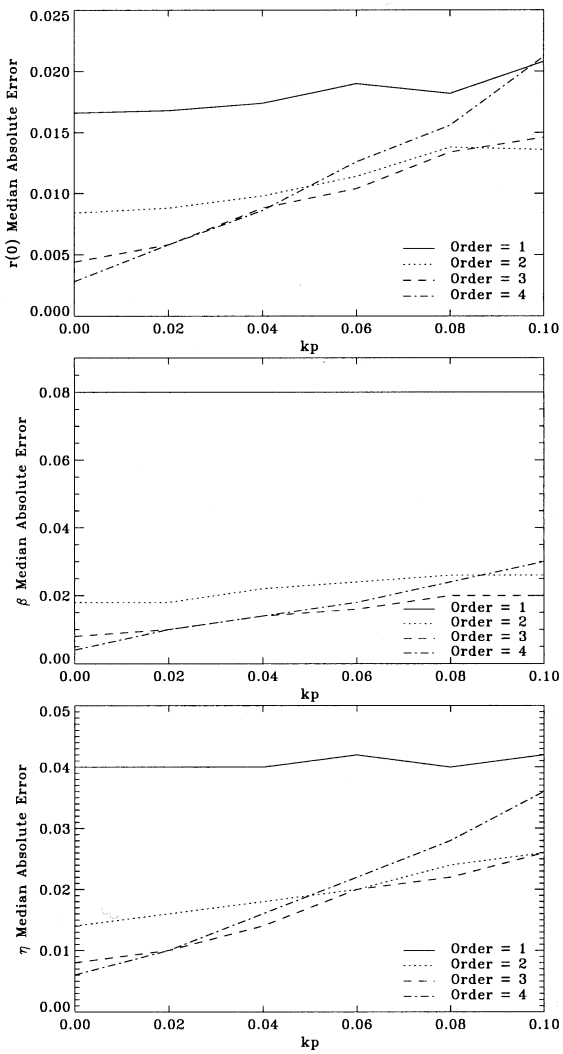

Fig. 9. Median absolute error of (top) $r(0)$, (middle) β, and (bottom) η estimates as a function of measurement noise parameter k_p and model order.

inputs. In actual scatterometer image reconstructions, such ideal incidence angle sampling is not common. For six-day NSCAT images generated at the SIR and AVE spatial resolutions of 4.45 km, average pixel regions usually encounter at least ten hits. Hence, for the remaining simulations, incidence angle sampling is performed randomly from a uniform distribution between 20° and 60° with ten samples for each realization. In addition, measurement noise is simulated using (9) and various k_p values. Typical NSCAT k_p levels are in the range 0 to 0.1. In fact, for the NSCAT Antarctic v-pol data collected from 1996 days 270–275, 97% of the k_p values are below 0.1 and 86% are below 0.05.

To offer more comprehensive simulations that consider a broad range of ($r(0)$, β, η) triplet combinations, synthetic "ground truth" images are constructed of each parameter that represent all possible sample combinations of the parameters within the ranges

$$r(0) \in [0.01, 0.3]$$
$$\beta \in [0.05, 0.4]$$
$$\eta \in [0.05, 0.4].$$

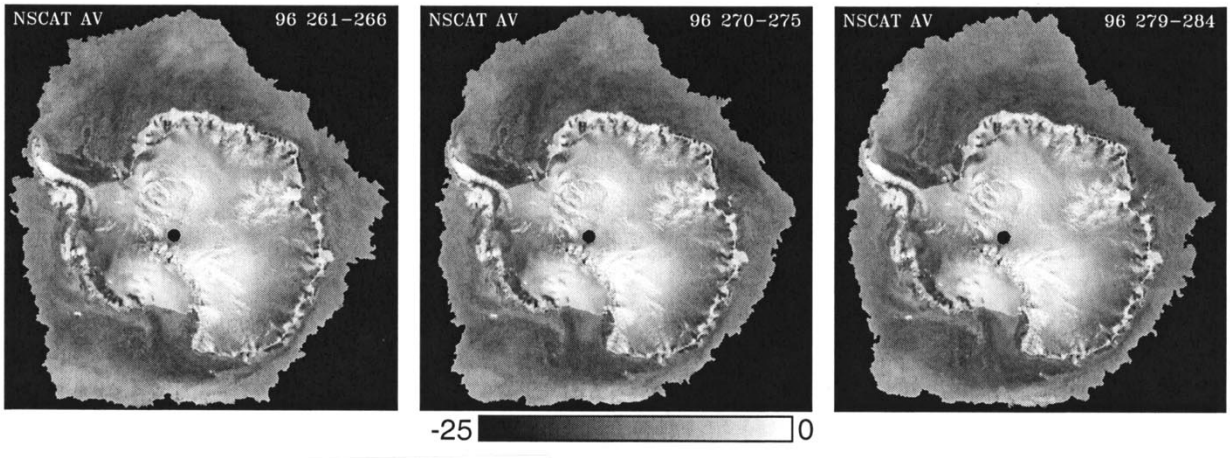

Fig. 10. Ice-masked NSCAT Antarctic A_v SIR image series.

These values represent ranges that cover typical sea ice surface parameters. The images are generated using 25 evenly spaced samples of each parameter resulting in 25^3 combinations. Fig. 5 shows the truth images that are used in the simulation process. Noise-corrupted polynomial coefficient images are simulated, which become inputs to the inverse model.

The simulations are run using the incidence angle sample scheme described previously. Noise levels (k_p) are considered at 0.02 increments from 0 to 0.1. The results are summarized graphically in Figs. 6–8. In Fig. 6, the $r(0)$ estimates are shown with k_p values of 0, 0.04, and 0.08. The image frames demonstrate increasing ability in the algorithm to accurately represent the left-to-right increasing gradient as the model order increases. Nearly all images show that the algorithm has difficulty in areas corresponding with very low β values. As previously noted, extremely low β correspond to scattering responses that are primarily contained below the 20° incidence angle limit for NSCAT data. The images also exhibit that higher order models are increasingly sensitive to noise as evident by the speckling in the estimate frames. Thus, a trade off exists between ability to estimate parameters accurately (on average) and sensitivity to measurement noise.

The performance of the algorithm in estimating β is shown in Fig. 7. The image panels reveal that first-order coefficients are not sufficient to accurately represent the surface roughness induced characteristics of the forward-scattering model. The first-order frames are nearly constant in value. In contrast, the second to fourth-order models are much more successful in reproducing the upward β gradients in the truth image. Like $r(0)$, the β estimates are increasingly sensitive to noise as order increases.

Estimates of the final parameter, η, are shown in Fig. 8. Similar trends with order exist for η estimates as with the previous two. The first-order model has difficulty generating the constant frames in the truth image. However, all of the higher order models appear to perform relatively well.

In order to provide a quantitative measure of algorithm performance over all the possible parameter combinations, the median absolute error is used. This metric is computed for each parameter as the median of the ensemble of absolute errors over the entire truth image. The estimate images have few very large errors caused by poor sampling or extreme noise. However, the few outliers can skew an average error metric. The median absolute error is used to reduce the confusing effects of these outliers.

Fig. 9 illustrates the error metric for the three forward-scattering model parameter estimates as a function of k_p. All of the plots indicate that parameter estimate error is lower for higher order models in the absence of noise. However, as k_p rises, the second or third-order estimates have the lowest median absolute error. The curves also show that higher order models are increasingly sensitive to k_p, evident in steeper slopes in the error plots. The first-order model is relatively insensitive to k_p in all three figures since this model performs the most averaging. From the results in Fig. 9, we conclude that the second- or third-order σ° versus θ polynomial coefficients provide the best inputs to the inverse model in the presence of noise. Since both offer similar error characteristics, the second-order model is used with actual NSCAT data as presented in the following section.

VI. Results

The inversion method is applied to second-order NSCAT reconstructed v-pol AVE imagery (A_v, B_v, and C_v) to study the behavior of the technique and to interpret phenomena observed in the reconstruction σ° images. First, the inversion is performed on Antarctic image sequences. Three six-day Antarctic SIR images are shown in Fig. 10. While the inversion is performed on third-order AVE imagery, enhanced resolution SIR A_v images are shown here for illustrative purposes. The differences between the SIR and AVE algorithm products are discussed above. The images are ice masked using an NSCAT-derived ice edge algorithm [9]. The three frames each show significant σ° detail within the ice pack. The goal of the inversion is to extract useful surface features from these variations and to provide maps of them. However, in this discussion we restrict ourselves to a few general observations in supplement to other studies, e.g., [31]. An interesting phenomenon illustrated by this image sequence is the "blooming" of σ° values near the ice perimeter. That is, the A_v values increase significantly in a very short period of

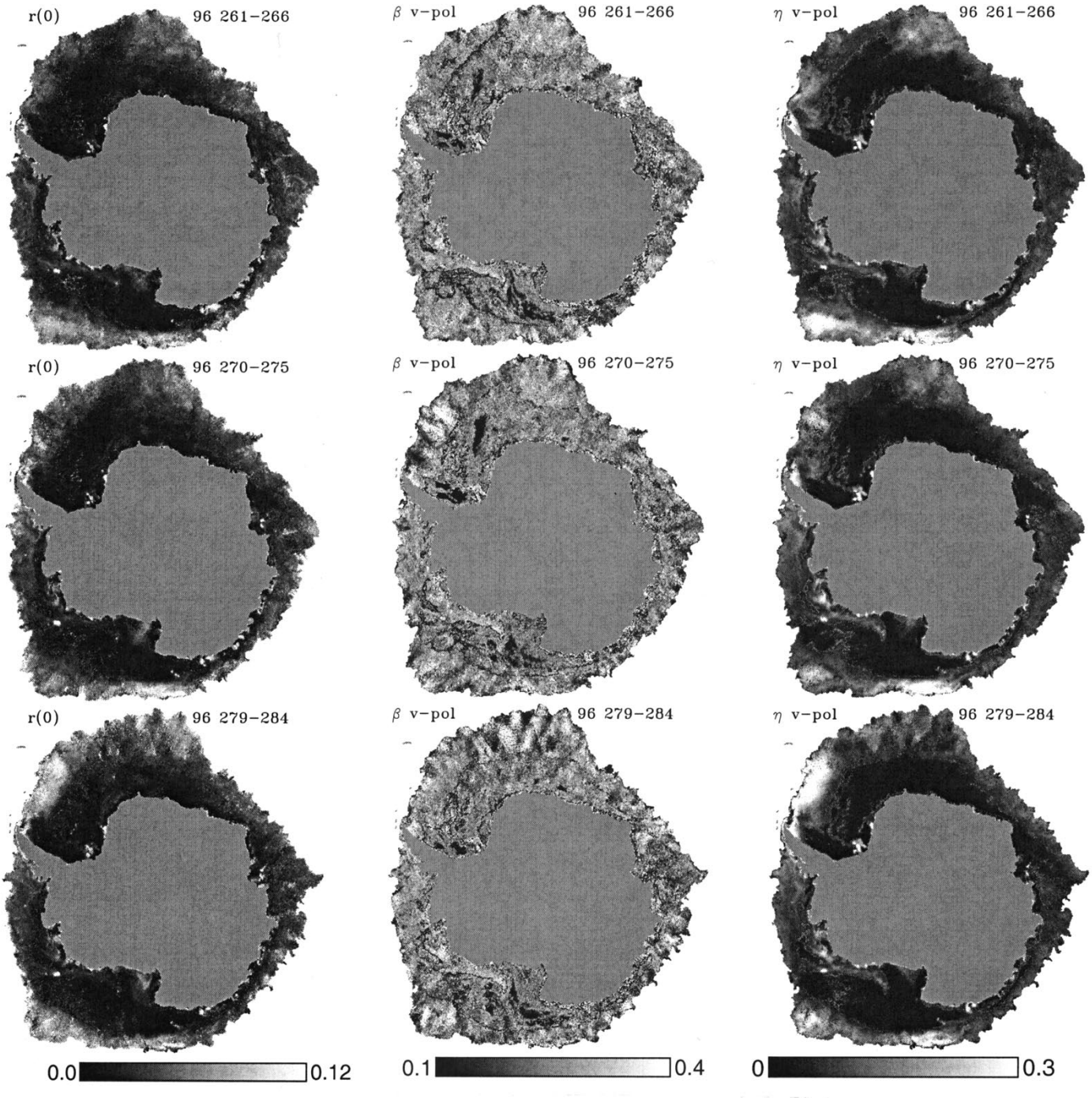

Fig. 11. Inverse model estimates of Antarctic. (Left column) $r(0)$. (Center column) β. (Right column) η.

time in localized regions. An example is shown near the ice edge in the outer Weddell Sea. The location of the Weddell Sea and the Ronne Ice Shelf (to be discussed below) are indicated in the first frame of Fig. 1. The A_v values in this region during the day 279–284 image are significantly higher than the previous two images. Special Sensor Microwave/Imager (SSM/I) radiometer brightness temperatures drop significantly in the bloom area. As described below, the inverse model is used to provide a physical interpretation of this phenomenon.

The inverse model is implemented for the Antarctic AVE image sets corresponding to the images in Fig. 10. Fig. 11 shows the spatial distribution of $r(0)$ estimates for each time interval. Several large ice bergs with very high $r(0)$ values are clearly observed in the images such as B10A in the lower-left quadrant of the image and several grounded ice bergs near the eastern limit of the Ronne Ice Shelf. First-year ice dominates much of the Antarctic ice pack. These regions have typically low $r(0)$ levels compared with ice bergs and several regions near the ice edge. The Weddell Sea bloom is evident in increased $r(0)$ indicating an increase in the effective permittivity.

The β estimates in Fig. 11 are visually more noisy than $r(0)$. Areas of very smooth first-year ice have low β values in the

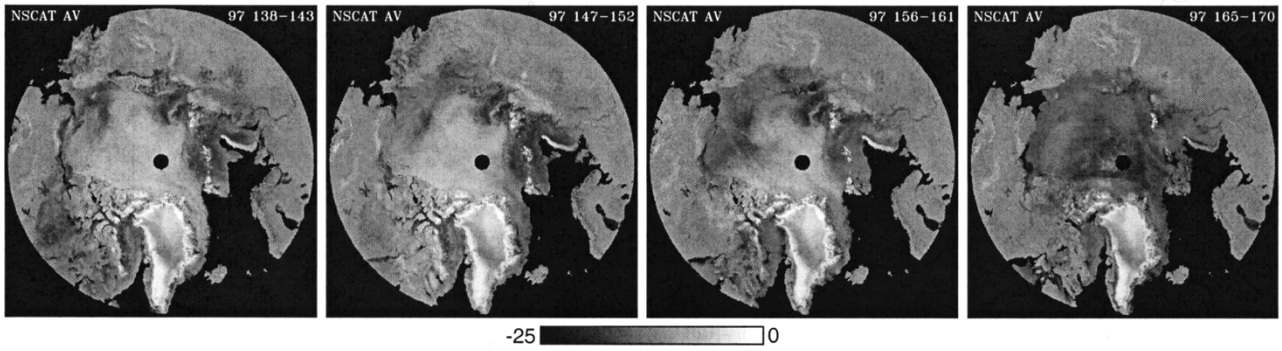

Fig. 12. Ice-masked NSCAT Arctic A_v SIR image series.

images. One example is near the western edge of the Ronne ice shelf, which is a region of new ice growth as older ice forms are drawn northward along the peninsula by the Weddell Gyre. The area surrounding the previously discussed grounded bergs have high β consistent with sea ice deformations caused as the ice pack collides with the bergs. The bloom area does not indicate any obvious change in this parameter.

The η parameter images are also shown in Fig. 11. The highest volume scattering albedo values are found in pixels covering ice bergs. Since ice bergs are composed of glacial ice, they have virtually no salinity and, thus, low loss. Microwave frequency pulses, therefore, are sensitive to scattering from subsurface inhomogeneities. A small region of multiyear ice near the tip of the peninsula also appears very bright in the image. A narrow stream of older deformed ice with medium η values is also evident running through the middle of the Weddell Sea parallel to the Ronne Ice Shelf. This line is created by the Weddell Gyre motion pulling ice debris away from the grounded ice bergs near the shelf. Much of the remaining ice pack, consisting primarily of various forms of first-year ice, have low volume scattering albedo. The only exceptions to this are in various bloom regions. In the final image, increased A_v in the Weddell bloom area is accompanied by a sudden rise in η. A local refreezing event could cause the observed change in volume scattering.

The inversion method is also applied to Arctic data. A four AVE image set series representing the onset of Arctic summer is used as inverse model inputs. The SIR ice-masked image series corresponding to the AVE imagery actually used in the inversion is illustrated in Fig. 12. As with the Antarctic case, SIR images are shown though AVE imagery are used in the inversion. The reconstructed SIR images exhibit greater detail in the A_v and A_h images, but are more susceptible to imaging artifacts that make them less desirable than their AVE counterparts for use in the inversion. The Arctic ice pack is characterized by large regions of multiyear ice exhibiting high A_v values near the centers of the images. Younger forms of ice have lower A_v signatures. The phenomenon examined in this sequence is the annual drop in σ° observations due to the passage of warm fronts over the ice pack inducing significant surface melting. While the first images have high multiyear σ° signatures differentiating this ice type from lower σ° first-year ice, by the end of the image sequence the two types are indistinguishable.

Fig. 13 contains the image estimates of Arctic $r(0)$. We note that the noisy values near the pole are due to insufficient incidence angle sampling caused by satellite orbit geometry and the NSCAT measurement collection configuration. Unsatisfactory sampling of the incidence angle spectrum results in poor estimates of polynomial fit coefficients in the image reconstruction. Consequently, very low confidence is placed on the near-pole parameter estimates. For comparison, SSM/I-derived multiyear and first-year ice concentration images are presented in Fig. 14 for the first Arctic image in the set (1997 days 138–143). These were produced by the NASA Team algorithm and were obtained from the National Snow and Ice Data Center (NSIDC). The general trend in the $r(0)$ imagery consists of relatively high and low values for multiyear and first-year sea ice, respectively. The melt event causes $r(0)$ to drop quickly over the entire multiyear area.

The distribution of β surface roughness values are shown in Fig. 13. Comparison with the ice concentration imagery of Fig. 14 illustrates that multiyear ice has typically high β levels in contrast to lower observations over first-year ice. Newer ice forms are typically less deformed than old ice that has been subjected to wave deformation, ice pack shearing, and large-scale roughness caused by melt/refreeze cycles. As the sequence progresses, β values drop until nearly the entire multiyear region appears similar to the first-year β observations. The source of the change may be due to surface smoothing of features due to melting and the creation of melt ponds, [6], [10].

The estimate images of Arctic volume scattering albedo η shown in Fig. 13 illustrate the intense volume scattering contributions characteristic of multiyear ice. Varying levels of η within multiyear regions can be related to the number density of volume scatterers and mean volume scattering element cross sections. Areas of younger ice have much lower η due to higher salinity and dielectric loss. The image progression shows η decreasing as temperature rises and surface melting occurs. In the last image frame, volume scattering has been almost completely masked by increased water content that reduces penetration depth. Such signatures masking makes the various ice types completely indistinguishable at Ku-band.

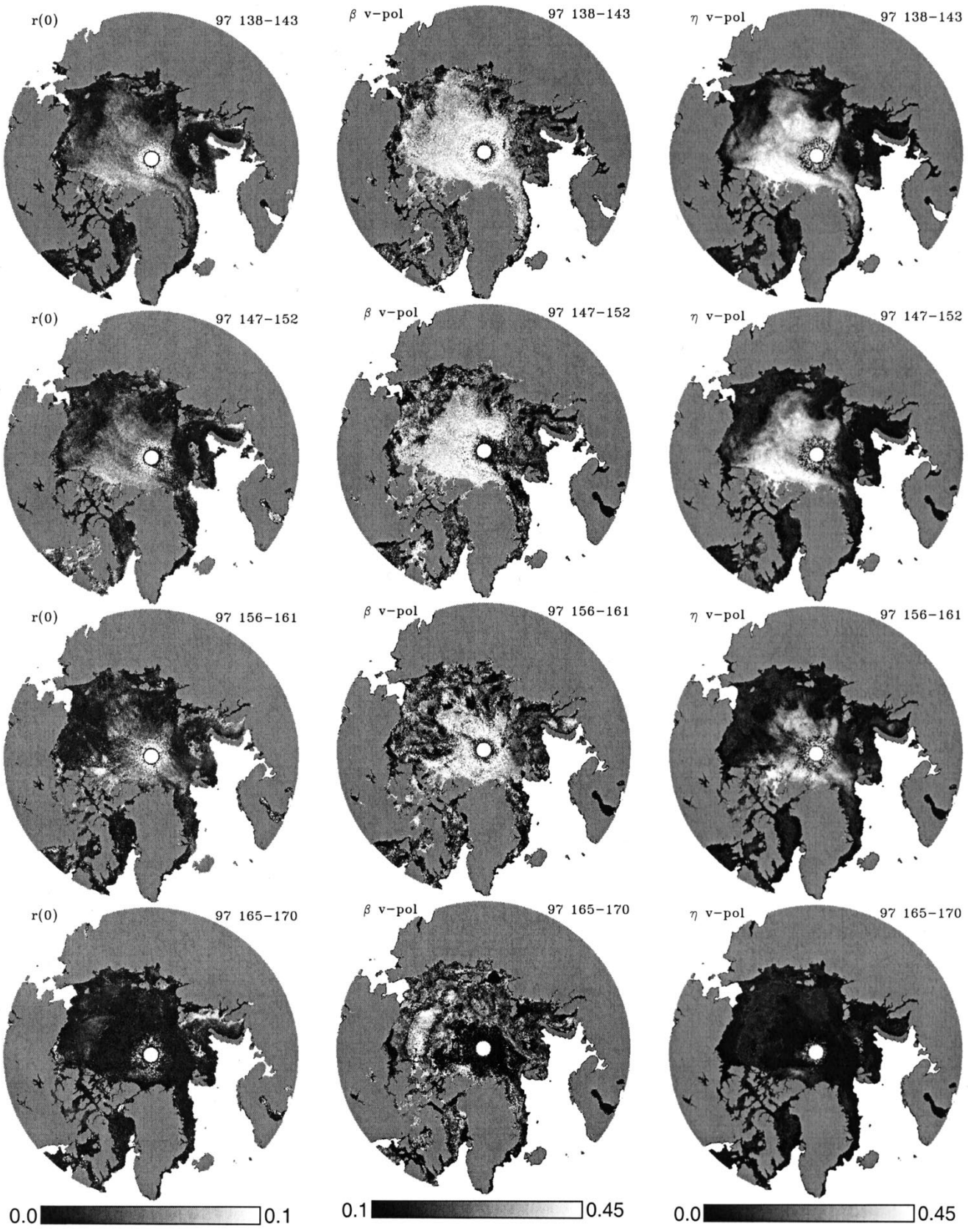

Fig. 13. Inverse model estimates of Arctic (Left column) $r(0)$. (Center column) β. (Right column) η.

These results illustrate the utility of the inverse model in interpreting the sources of scattering phenomena observed in reconstructed NSCAT imagery. Since the model inversion method is fully automated, large ensembles of measurements can be inverted providing estimates of the spatial distribution and magnitude of important surface parameters. These parameters can then

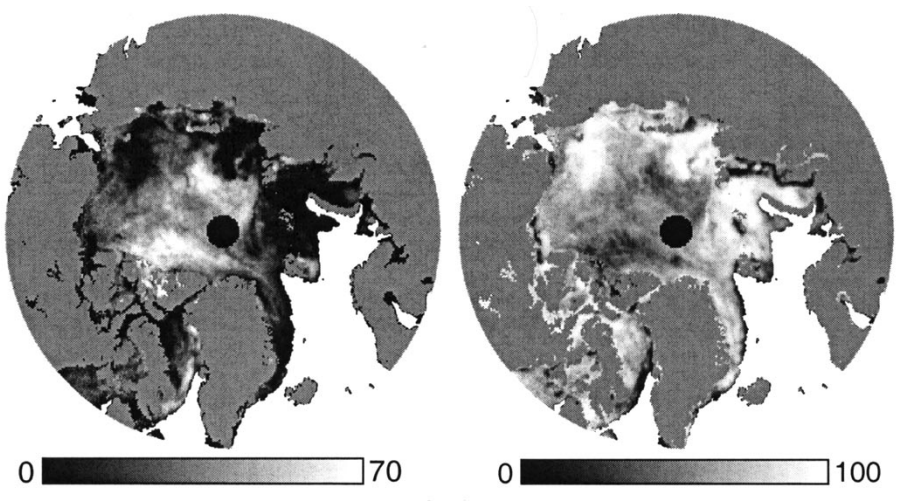

Fig. 14. NSIDC SSM/I-derived multiyear (left) and first-year (right) Arctic sea ice concentration images for 1997 days 138–143.

be related to sea ice types as previously described. In general, older ice types such as multiyear ice exhibit very high $r(0)$ and η values in the absence of significant surface melt. In contrast, first-year ice and other relatively young ice types have much lower $r(0)$ and η. Smoother ice types have typically lower β levels. Temporal variations in the parameters can be used to understand the evolution of scattering mechanisms within the various ice types as considered in this section.

VII. Conclusion

This study has presented an inversion technique applied to a simple, but robust forward-scattering model. The method is fully automated requiring no user interface. Consequently, large scatterometer polynomial fit coefficient images representing the incidence angle dependence of σ° can be used as inputs to the inverse model. The algorithm is used to determine the spatial distribution of three important surface parameters: the power reflection coefficient at nadir, $r(0)$, the rms surface slope, S (represented by $\beta = 2S^2$ in the inverse model), and the volume scattering albedo, η.

Simulations of the method demonstrate the capability of the algorithm. Higher order incidence angle dependence models yield better estimates of the surface parameters in the absence of noise. When noise is introduced, a trade-off exists between the capability to estimate a wide range of possible parameter combinations and sensitivity to noise. The first-order model performs reasonably well for $r(0)$ and η estimation but cannot effectively reproduce true β values. A good balance is found in using a second-order model.

The inverse model is applied to NSCAT Antarctic and Arctic image sequences. The results show that the parameter images have consistent spatial distributions. The image products are used to interpret σ° "blooming" phenomena in the Antarctic. An increase in $r(0)$ and η is observed in the bloom regions with little change in β. The method is also used to analyze drastic σ° decreases over multiyear ice in the Arctic as the summer season begins. The accompanying surface melt causes all three parameters to decrease abruptly. Surface roughness appears to be reduced and increased water content masks the volume scattering contribution that give multiyear ice its characteristically high σ° signature.

The results of this study demonstrate the utility of one technique in inverting simple forward-scattering models for sea ice surfaces. Validation data of surface roughness parameters, dielectric properties, and volume scattering element characteristics are needed to accurately measure the algorithm's effectiveness. Unfortunately, access to suitable validation data over such large areas for this initial study was very limited and thus further work is required. Regardless, the method can aid in the interpretation of important polar geophysical phenomena.

Acknowledgment

NSCAT data were provided by the Jet Propulsion Laboratory DAAC. SSM/I-derived Arctic and Antarctic ice concentrations were obtained from the NSIDC.

References

[1] W. F. Budd, "Antarctic sea ice variations from satellite sensing in relation to climate," *IEEE Trans. Geosci. Remote Sensing*, vol. GE-15, pp. 417–426, 1975.

[2] F. D. Carsey, Ed., *Microwave Remote Sensing of Sea Ice*. Washington, DC: Amer. Geophys. Union, 1992.

[3] D. Long and M. Drinkwater, "Greenland ice-sheet surface properties observed by the Seasat-A scatterometer at enhanced resolution," *J. Glaciol.*, vol. 40, no. 135, pp. 213–230, 1994.

[4] M. R. Drinkwater and D. G. Long, "Seasat, ERS-1/2 and NSCAT scatterometer observed changes on the large ice sheets," in *Proc. IGARSS*, vol. 4, Seattle, WA, July 6–10, 1998, pp. 2252–2254.

[5] M. R. Drinkwater and F. D. Carsey, "Observations of the late-summer to fall transition with the 14.6 GHz SEASAT scatterometer," in *Proc. IGARSS*, vol. 3, Espoo, Finland, June 3–6, 1991, pp. 1597–1600.

[6] C. P. Winebrenner, D. G. Long, and B. Holt, "Mapping the progression of melt onset and freeze-up on arctic sea ice using SAR and scatterometry," in *Analysis of SAR Data of the Polar Oceans*, C. Tsatsoulis and R. Kwok, Eds. Berlin, Germany: Springer-Verlag, 1998, pp. 129–144.

[7] Q. P. Remund and D. G. Long, "An iterative approach to multisensor sea ice classification," *IEEE Trans. Geosci. Remote Sensing*, vol. 38, pp. 1843–1856, July 2000.

[8] F. Gohin and A. Cavanie, "A first try at identification of sea ice using the three beam scatterometer of ERS-1," *Int. J. Remote Sens.*, vol. 15, no. 6, pp. 1221–1228, 1994.

[9] Q. P. Remund and D. Long, "Sea-ice extent mapping using Ku-band scatterometer data," *J. Geophys. Res*, vol. 104, no. C4, pp. 11 515–11 527, 1999.

[10] D. G. Long and M. R. Drinkwater, "Cryosphere applications of NSCAT data," *IEEE Trans. Geosci. Remote Sensing*, vol. 37, pp. 1671–1684, May 1999.
[11] M. R. Drinkwater and X. Liu, "Observing interannual variability in sea-ice dynamics using NSCAT," in *Proc. NSCAT Science Team Workshop*. Pasadena, CA, Jan. 23–24, 1997, JPL Tech. Pub..
[12] Q. P. Remund and D. G. Long, "Iterative mapping of polar sea ice using Ku-band seawinds scatterometer data," *IEEE Trans. Geosci. Remote Sensing*, 2002, submitted for publication.
[13] F. Carsey, "Review and status of remote sensing of sea ice," *IEEE J. Oceanic Eng.*, vol. 14, pp. 127–137, Apr. 1989.
[14] D. J. Cavalieri, J. P. Crawford, M. R. Drinkwater, D. T. Eppler, L. D. Farmer, R. R. Jentz, and E. C. Wackerman, "Aircraft active and passive microwave validation of sea ice concentration from the Defense Meteorological Satellite Program Special Sensor Microwave Imager," *J. Geophys. Res.*, vol. 96, no. C12, pp. 21 989–22 008, 1991.
[15] D. J. Cavalieri, P. Gloersen, and W. J. Campbell, "Determination of sea ice parameters with the Nimbus-7 SMMR," *J. Geophys. Res.*, vol. 89, no. D4, pp. 5355–5369, 1984.
[16] J. W. Rouse, "Arctic ice type identification by radar," *Proc. IEEE*, vol. 57, pp. 605–611, Apr. 1969.
[17] R. Kwok, E. Rignot, B. Holt, and R. Onstott, "Identification of sea ice types in spaceborne synthetic aperture radar data," *J. Geophys. Res.*, vol. 97, no. C2, pp. 2391–2402, 1992.
[18] M. Golden, D. Borup, M. Cheney, E. Cherkaeva, M. S. Dawson, K. Ding, A. K. Fung, D. Isaacson, S. A. Johnson, A. K. Jordan, J. A. Kong, R. Kwok, S. V. Nghiem, R. G. Onstott, J. Sylvester, D. P. Winebrenner, and I. H. H. Zabel, "Inverse electromagnetic scattering models for sea ice," *IEEE Trans. Geosci. Remote Sensing*, vol. 36, pp. 1675–1705, Sept. 1998.
[19] F. M. Naderi, M. H. Freilich, and D. G. Long, "Spaceborne radar measurement of wind velocity over the ocean—An overview of the NSCAT scatterometer system," *Proc. IEEE*, vol. 79, pp. 850–866, June 1991.
[20] D. Long, P. Hardin, and P. Whiting, "Resolution enhancement of spaceborne scatterometer data," *IEEE Trans. Geosci. Remote Sensing*, vol. 31, pp. 700–715, May 1993.
[21] D. S. Early and D. G. Long, "Image reconstruction and enhanced resolution imaging from irregular samples," *IEEE Trans. Geosci. Remote Sensing*, vol. 39, pp. 291–302, Feb. 2001.
[22] Q. P. Remund and D. G. Long, "Validation of the SIRF resolution enhancement algorithm for scatterometer data using SAR imagery," in *Proc. IGARSS*, vol. 2, Hamburg, Germany, June 28–July 2 1999, pp. 1309–1311.
[23] J. K. Lee and J. A. Kong, "Active microwave remote sensing of an anisotropic random medium layer," *IEEE Trans. Geosci. Remote Sensing*, vol. GE-23, pp. 910–923, Nov. 1985.
[24] S. Tjuatja, A. K. Fung, and J. Bredow, "A scattering model for snow-covered sea ice," *IEEE Trans. Geosci. Remote Sensing*, vol. 30, pp. 804–810, July 1992.
[25] S. V. Nghiem, R. Kwok, S. H. Yueh, and M. R. Drinkwater, "Polarimetric signatures of sea ice, theoretical model," *J. Geophys. Res.*, vol. 190, no. C7, pp. 13 665–13 679, 1995.
[26] F. T. Ulaby, R. K. Moore, and A. K. Fung, *Microwave Remote Sensing—Active and Passive*. Norwood, MA: Artech House, 1985, vol. 3.
[27] C. T. Swift, "Seasat scatterometer observations of sea ice," *IEEE Trans. Geosci. Remote Sensing*, vol. 37, pp. 716–723, Mar. 1999.
[28] C. T. Swift, P. E. Hayes, J. S. Herd, W. L. Jones, and V. E. Delnore, "Airborne microwave measurements of the southern Greenland ice sheet," *J. Geophys, Res.*, vol. 90, no. B2, pp. 1983–1994, February 1985.
[29] D. E. Barrick, "Rough surfaces," in *Radar Cross-Section Handbook*, G. T. Ruck, Ed. New York: Plenum, 1970, pp. 671–772.
[30] M. R. Vant, R. O. Ramseier, and V. Makois, "The complex dielectric constant of sea ice at frequencies in the range 0.1–40 GHz," *J. Appl. Phys.*, vol. 49, pp. 1264–1280, 1978.
[31] M. R. Drinkwater and V. I. Lytle, "ERS-1 SAR and field-observed characteristics of austral fall freeze-up in the Weddell Sea, Antarctica," *J. Geophys. Res.*, vol. 102, no. C6, pp. 12 593–12 608, 1997.

Quinn P. Remund (S'89–M'90) received the B.S. and Ph.D. degrees in electrical and computer engineering from Brigham Young University, Provo, UT, in 1996 and 2000.

He is currently with Ball Aerospace and Technologies, Corporation, Boulder, CO.

David G. Long (S'80–SM'98) received the Ph.D. degree in electrical engineering from the University of Southern California, Los Angeles, in 1989.

From 1983 to 1990, he was with the National Aeronautics and Space Administration (NASA) Jet Propulsion Laboratory (JPL), Pasadena, CA, where he developed advanced radar remote sensing systems. While at JPL, he was the Senior Project Engineer on the NASA Scatterometer (NSCAT) project, which was flown aboard the Japanese Advanced Earth Observing System (ADEOS) from 1996 to 1997. He is currently a Professor in the Electrical and Computer Engineering Department, Brigham Young University, Provo, UT, where he teaches upper division and graduate courses in communications, microwave remote sensing, radar, and signal processing. He is the Principle Investigator on several NASA-sponsored interdisciplinary research projects in microwave remote sensing and innovative radar systems. He has numerous publications in signal processing and radar scatterometry. His research interests include microwave remote sensing, estimation theory, signal processing, and mesoscale atmospheric dynamics.